CrossMark

Inertial Effects on the Vertical Transport of Suspended Particles in a Turbulent Boundary Layer

David Richter[1] · **Marcelo Chamecki**[2]

Abstract In many atmospheric flows, a dispersed phase is actively suspended by turbulence, whose competition with gravitational settling ultimately dictates its vertical distribution. Examples of dispersed phases include snow, sea-spray droplets, dust, or sand, where individual elements of much larger density than the surrounding air are carried by turbulent motions after emission from the surface. In cases where the particle is assumed to deviate from local fluid motions only by its gravitational settling (i.e., they are inertialess), traditional flux balances predict a power-law dependence of particle concentration with height. It is unclear, however, how particle inertia influences this relationship, and this question is the focus of this work. Direct numerical simulations are conducted of turbulent open-channel flow, laden with Lagrangian particles of specified inertia; in this way the study focuses on the turbulent transport which occurs in the lowest few meters of the planetary boundary layer, in regions critical for connecting emission fluxes to the fluxes felt by the full-scale boundary layer. Simulations over a wide range of particle Stokes number, while holding the dimensionless settling velocity constant, are performed to understand the role of particle inertia on vertical dispersion. It is found that particles deviate from their inertialess behaviour in ways that are not easily captured by traditional theory; concentrations are reduced with increasing Stokes number. Furthermore, a similarity-based eddy diffusivity for particle concentration fails as particles experience inertial acceleration, precluding a closed-form solution for particle concentration as in the case of inertialess particles. The primary consequence of this result is that typical flux parametrizations connecting surface emission models (e.g., saltation models or sea-spray generation functions) to elevated boundary conditions may overestimate particle concentrations due to the reduced vertical transport caused by inertia in between; likewise particle emission may be underestimated if inferred from concentration measurements aloft.

✉ David Richter
David.Richter.26@nd.edu

Marcelo Chamecki
chamecki@ucla.edu

[1] University of Notre Dame, Notre Dame, IN, USA

[2] University of California Los Angeles, Los Angeles, CA, USA

⚡ Springer

1 Introduction

The planetary boundary layer (PBL) links the earth's surface to the atmosphere, and as a result controls the transmission of dust, salt, and other aerosols from their emission source at the surface to the larger mesoscale and synoptic-scale motions that govern their long-range transport and ultimate fate. Once airborne, these particulates can alter key chemical (O'Dowd and de Leeuw 2007), optical (Kleefeld et al. 2002), and meteorological (Rosenfeld et al. 2008) processes before being deposited back onto the terrestrial or marine surface. Thus much work has been done in understanding and accurately parametrizing near-surface particle emission and transport processes for use in weather and climate prediction models, however continued discrepancies between models and observations remain a challenge (Reid et al. 2006; Knippertz and Todd 2012). For instance, aircraft observations of large (up to 300 μm) sand grains above the Saharan Desert (Rosenberg et al. 2014) are in apparent contradiction with the upper limit of standard saltation models (Kok 2011).

The difficulty of developing dust and aerosol emission schemes is due largely to unresolved, small-scale, and process-specific details, such as those resulting from wave breaking (Lewis and Schwartz 2004) or saltation (Anderson and Haff 1988). In this regard, the present work focuses on understanding the details of turbulent particle transport within the atmospheric surface layer (ASL)—in particular the vertical flux of large particles that are heavy (i.e., they experience gravitational settling) and inertial (i.e., they do not necessarily follow fluid streamlines). It is the latter consideration, that of particle inertia, which is often neglected in particle flux parametrizations since even large sand grains or water droplets do indeed appear inertialess relative to PBL-scale motions. Our work is focused, however, on turbulent transport that occurs in the lowest layers of the ASL (a few metres above the surface), a region that plays a crucial role in connecting surface particle emission to transport throughout the full PBL, and where particle inertia can be non-negligible in their transport characteristics.

Attempts to parametrize heavy particle transport can begin by first approximating the suspended particulate as a passive scalar, in which case the horizontally-averaged vertical concentration profile and its relation to the surface flux is described by Monin–Obukhov (MO) similarity theory (Monin and Yaglom 1971). The particles can be made more realistic by adding a non-zero and constant settling velocity, which yields a power-law vertical profile under neutral conditions assuming that the turbulent diffusivity of particle concentration is proportional to that of momentum (Rouse 1937; Prandtl 1952), and reflects an equilibrium balance between suspension via turbulence and gravitational settling. Other modifications, including disequilibrium between gravitational settling and turbulent suspension (Chamberlain 1967; Kind 1992), heterogeneous surface fluxes (Chamecki and Meneveau 2011; Pan et al. 2013), non-neutral atmospheric stability (Freire et al. 2016), or various other meteorological effects specific to, for instance, sea-salt aerorols (Toba 1965) or snow (Pomeroy and Male 1992), can be made as well.

It is well-known that particle inertia can lead to phenomena in turbulent flows such as preferential clustering (Rouson and Eaton 2001) or turbophoretic drift [i.e., a net flux down a gradient of turbulent kinetic energy (TKE)] (Reeks 1983; Sardina et al. 2012), and these play a key role in determining inertial particle dispersion. For example, inhomogeneous horizontal particle distributions, such as those found in sand streamers (Baas 2008), may

disrupt typical key assumptions, though these can be captured in large-eddy simulation (LES) (Groot Zwaaftink et al. 2014). Much effort has gone into understanding inertial particle transport in turbulent channel flows, relating particle dynamics with turbulent events such as sweeps and ejections (Righetti and Romano 2004; Soldati and Marchioli 2009) or relating the modulation of turbulence to suspended particles (Vreman 2015), but many of these studies neglect the effects of wall-normal gravitational settling. In the presence of gravitational settling, particle clustering can lead to enhancements of the effective particle settling velocity (Wang and Maxey 1993; Aliseda et al. 2002), where the average downwards particle velocity component exceeds the still-air settling velocity as predicted by, say, Stokes drag.

In the PBL, while many theoretical and computational attempts have been made to characterize the Lagrangian dispersion characteristics of particles in turbulence (Csanady 1963; Wang and Stock 1993), it remains unclear how these effects of particle inertia modify the flux-profile relationship of particle mass concentration in the PBL, particularly in the lowest layers near the surface where Stokes numbers can be non-negligible. Even in theoretical studies devoted to the topic of vertical particle dispersion that attempt to include inertia, such as Belan et al. (2016), restrictions are necessarily made regarding the degree of particle inertia and the regions of the flow where the corrections are valid. Furthermore, in the well-known conceptual model for dry deposition (Slinn and Slinn 1980; Slinn 1982), the overall deposition velocity of particulate matter is represented as a series of resistances to vertical transport, including turbulence, molecular diffusion, and (when applicable) vegetative canopies. This conceptual model is the basis for many studies that aim to link surface emission to concentrations measured aloft—see, for example, Hoppel et al. (2002) or Fairall and Larsen (1984)—and within this framework particle inertia is only occasionally considered (Peters and Eiden 1992; Zhang et al. 2001). When inertia is indeed included, it is only in the form of so-called inertial impaction, the process by which particles can efficiently travel through the diffusive sublayer due to inertia, thereby reducing the diffusive resistance to deposition.

The aim of the present study is to therefore investigate the role of particle inertia on modifying concentration profiles and vertical fluxes in the lowest few metres of the PBL. This is done using an idealized approach based on direct numerical simulation (DNS), and focuses on the flux-profile relationship and potential modelling strategies. It is ultimately demonstrated that particle inertia can reduce turbulent fluxes of particle concentration, which can create a disconnect between true surface emission fluxes and fluxes into the full PBL. In some sense this is akin to an additional inertial resistance layer in the conceptual model of Slinn and Slinn (1980), and may potentially produce miscalculations of surface fluxes or the overprediction of suspended particulate matter.

2 Methodology

2.1 Numerical Simulation

2.1.1 Direct Numerical Simulation

We use DNS of turbulent open-channel flow, where Lagrangian particles are tracked individually. Details of the numerical method can be found in previous studies (Richter and Sullivan 2013, 2014; Helgans and Richter 2016), so only a brief summary is included here. The neutrally-stratified, incompressible Navier-Stokes equations are solved in a Cartesian domain using a pseudospectral discretization in the homogeneous, periodic x and y directions

and a second-order, finite difference discretization in the vertical, wall-normal z direction. Time integration occurs via a low-storage, third-order Runge–Kutta scheme (Spalart et al. 1991).

Mass and momentum conservation are given by

$$\frac{\partial u_i}{\partial x_i} = 0, \tag{1}$$

$$\frac{\partial u_i}{\partial t} + u_j \frac{\partial u_i}{\partial x_j} = -\frac{1}{\rho_f} \frac{\partial p}{\partial x_i} + \nu_f \frac{\partial^2 u_i}{\partial x_j^2}, \tag{2}$$

where u_i is the fluid velocity, ρ_f is the fluid density, and ν_f is the fluid kinematic viscosity. Incompressibility is enforced by solving a pressure Poisson equation at each Runge–Kutta stage. A no-slip condition is imposed at the lower domain wall, and a no-stress condition is imposed at the upper wall. The horizontal directions are periodic, and the flow is driven by a constant pressure gradient, chosen to produce turbulent open-channel flow with a Reynolds number of $Re_* = 300$, where $Re_* = u_* H / \nu_f$ is the friction Reynolds number based on the domain height H and the friction velocity $u_* = \sqrt{\tau_w / \rho_f}$ (τ_w is the wall stress).

At the same time, an advection-diffusion equation for a passive scalar is computed,

$$\frac{\partial C}{\partial t} + \frac{\partial}{\partial x_j} \left(v_j C \right) = \Gamma_C \frac{\partial^2 C}{\partial x_j^2}, \tag{3}$$

where Γ_C is the molecular diffusivity of scalar C. The concentration is advected by a velocity v_j, which is not necessarily equal to the local fluid velocity u_j. For instance, as done by Chamecki et al. (2009), this can be set to $v_j = u_j - w_s \delta_{j3}$ to represent uniform gravitational settling, where $w_s = \tau_p g$ is the single-particle particle terminal velocity specified by its inertial time constant τ_p and the magnitude of the acceleration due to gravity g, and δ_{j3} is the Kronecker delta. A truly passive scalar would have $v_j = u_j$. Herein, we assume a Schmidt number $Sc = \nu_f / \Gamma_C$ of unity. At the lower boundary, the Dirichlet condition $C \equiv C_0 = 1$ is held fixed, while at the upper boundary a no-flux condition is imposed. The domain is initialized with $C = 0$ at $t = 0$.

2.1.2 Lagrangian Particle Tracking

The primary goal is to characterize the effects of particle inertia on turbulent fluxes and vertical concentration profiles in a turbulent boundary layer, and this is readily accomplished using Lagrangian methods (see, e.g., Balachandar 2009). Thus each simulation is seeded with a large number of Lagrangian point particles, whose ensemble-averaged concentration field is the scalar C governed by Eq. 3. The particles are assumed to be one-way coupled, in that they do not have any influence on the surrounding flow, since we assume here that the mass fraction of suspended particles is sufficiently low. In air suspended with solid or liquid particles, this approximation holds if the mass loading is roughly 1% or below (Balachandar and Eaton 2010). Each particle obeys momentum conservation according to

$$\frac{dv_{p,i}}{dt} = \frac{1}{\tau_p} \left(u_{f,i} - v_{p,i} \right) - g \delta_{i3}, \tag{4}$$

where $v_{p,i}$ is the particle velocity, and $\tau_p = \rho_p d_p^2 / 18 \rho_f \nu_f$ is the Stokes time scale. In these expressions d_p is the particle diameter, $u_{f,i}$ is the fluid velocity interpolated to the particle location, and ρ_p is the particle density.
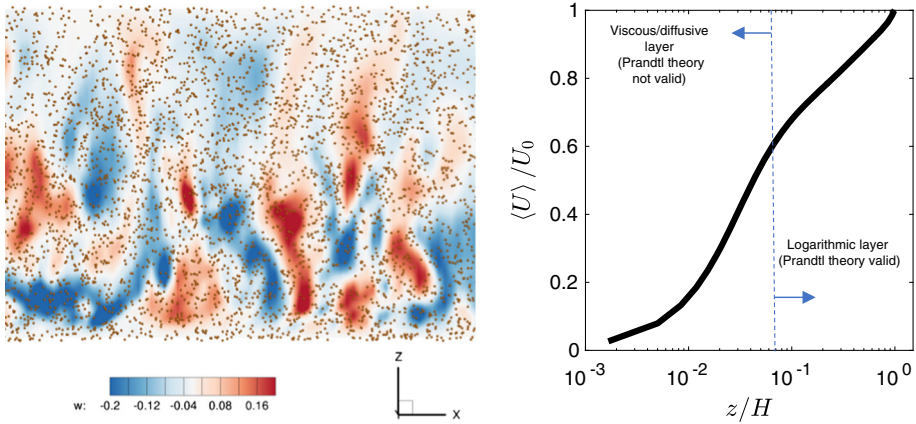
Fig. 1 Left: Snapshot of the computation. Colours reflect contours of fluctuating vertical velocity and brown dots represent Lagrangian particles. The z axis has been magnified by a factor of 2.5. Right: mean velocity profile, showing the existence of a logarithmic layer above $z/H \approx 0.1$

In the limit of inertialess particles (i.e., the Stokes number $St \to 0$, where $St = \tau_p/\tau_f$ and τ_f is a relevant flow time scale; here we use the Kolmogorov time scale τ_K), Eq. 4 is not solved and rather the particle velocity is simply equal to the local fluid velocity less its terminal velocity,

$$v_{p,i} = u_{f,i} - \tau_p g \delta_{i3} = u_{f,i} - w_s \delta_{i3}. \tag{5}$$

In the further limit of massless particles, in which case the particles would simply represent a discretized form of a continuous passive tracer field, the particle velocity is equal to the local fluid velocity: $v_{p,i} = u_{f,i}$.

Given the restriction to relatively low Reynolds numbers due to the use of DNS, molecular diffusion of both momentum and scalar C occurs in a non-negligible region near the walls. To provide equivalency between the Lagrangian representation (i.e., the particles) and the Eulerian field C, the particles are moved according to a combination of their advection velocity $v_{p,i}$ and a Brownian step chosen to provide a diffusivity Γ_C,

$$dx_{p,i} = v_{p,i}dt + \sqrt{2dt\,\Gamma_C}d\xi_i, \tag{6}$$

where $d\xi_i$ is a Weiner process representing Brownian motion. Numerically, advection is solved using the same RK3 method used for the flow, and at the end of each timestep, a random jump is added to provide the diffusive jump. Figure 1 provides a snapshot of the flow simulation with instantaneous particle location.

As noted above, the Eulerian scalar concentration C is held fixed at $C_0 = 1$ at the bottom wall, and a no-flux condition is imposed at the top wall. For Lagrangian particles, the same conditions are enforced: at the top wall, this means that particles are elastically reflected, and at the bottom wall, a reservoir of a constant number of particles just below the surface is maintained whose concentration is defined as $C_0 = 1$. The mean concentration $\langle C \rangle$ is then computed from a Lagrangian perspective at a specific height by counting the particles in the horizontal slab with volume $L_x \times L_y \times \Delta z$ (where L_x and L_y are the domain extents in the x and y directions and Δz is the vertical grid spacing at a particular height z) and normalizing with the concentration/volume combination maintained just below the bottom surface. This method requires a sufficient number of particles for statistical convergence of the particle
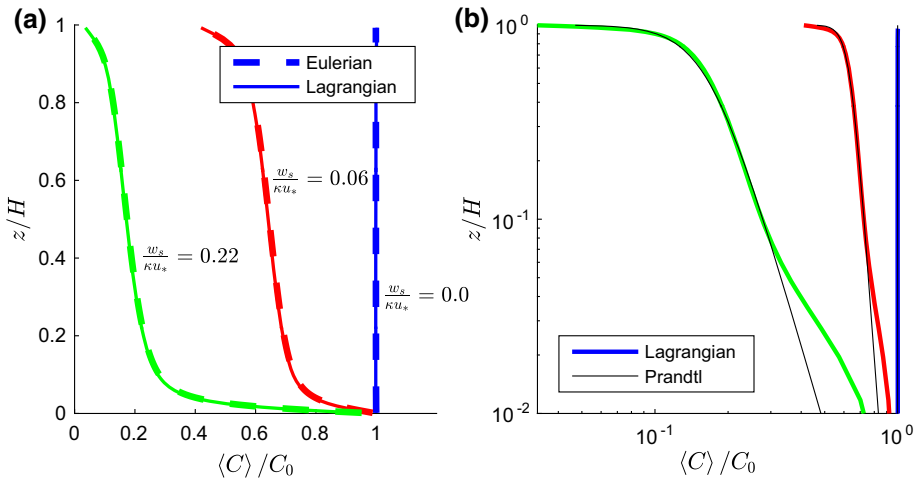
Fig. 2 Mean normalized particle concentration $\langle C \rangle / C_0$ versus normalized height z/H for three different settling velocities without inertia. Colours indicate different settling velocities and are indicated on the left. **a** Linear axes showing the comparison between the Eulerian solution (solid lines) and Lagrangian solution (dashed lines). **b** Logarithmic axes comparing the computed solutions to the Prandtl (1952) theory (Eq. 9)

averages, and in this case the number of particles maintained in the lower reservoir was held at 1×10^4 [this leads to particle numbers in the domain of $O(10^6)$].

Figure 2a shows a comparison between the Eulerian (Eq. 3) and Lagrangian prediction of $\langle C \rangle / C_0$ in the inertia-free case, for three different settling velocities. The settling velocities w_s are normalized by κu_* so that they reflect the settling tendency as compared to the strength of wall shear stress—in sediment transport literature this ratio is commonly referred to as the Rouse number (Rouse 1937). Figure 2a demonstrates the equivalence between the Eulerian and Lagrangian particle treatment, including the adjustment of the advection velocity v_i in Eq. 3 by the settling velocity.

2.2 Existing Theory

Following Prandtl (1952) (and many others since), the Reynolds decomposition $C = \langle C \rangle + c'$ can be introduced into Eq. 3, and after averaging the equations in the absence of particle inertia and a net surface flux (e.g., Kind 1992), one recovers a balance between turbulent suspension and gravitational settling,

$$\langle c'w' \rangle - \langle C \rangle w_s = 0. \tag{7}$$

If one then makes the assumption that the turbulent particle concentration flux $\langle c'w' \rangle$ can be expressed with an eddy diffusivity, in analogy with momentum and passive scalars, Eq. 7 becomes,

$$-K_C \frac{d \langle C \rangle}{dz} - \langle C \rangle w_s = 0, \tag{8}$$

where K_C is the eddy diffusivity. In the neutral ASL, Monin–Obukhov similarity theory implies $K_C = \kappa u_* z$ since the turbulent flux $\langle c'w' \rangle$ does not vary with height (here $\kappa = 0.41$ is the von Kármán constant and the turbulent Schmidt number is assumed to be unity). For

open-channel flow, however, the linearly varying momentum flux with height results in a parabolic diffusivity profile, given by $K_C = \kappa u_* z \left(1 - z/H\right)$ (see, e.g., Fischer 1973).

In its original formulation, the Prandtl solution to the ordinary differential equation of Eq. 8 suggests that the average concentration varies as a power-law with height, with an exponent of $w_s/(\kappa u_*)$. Using the open-channel version of K_C yields an equivalent result for systems where the total momentum flux varies linearly with height, which is a product of two power laws,

$$\frac{\langle C \rangle (z)}{C_r} = \left(\frac{z}{z_r}\right)^{-w_s/\kappa u_*} \left(\frac{z - H}{z_r - H}\right)^{w_s/\kappa u_*} \tag{9}$$

Here z_r is a constant reference height where the mean concentration is C_r ($z_r = 0.3H$ herein), and hereafter, the "Prandtl" solution refers to Eq. 9, although it represents a profile in an open-channel configuration where the eddy diffusivity K_C is parabolic with height, as opposed to the original ASL version (Prandtl 1952). As noted previously, throughout the literature (particularly in relation to sediment transport) this profile is occasionally referred to as the Rouse profile (Rouse 1937).

Figure 2b shows that the Prandtl solution of Eq. 9 agrees very well with the concentration profiles computed in the inertialess cases, above a height of $z/H \approx 0.1$. Below this height, molecular diffusivity plays a large role (since the simulations are based on DNS), violating the basic assumption that the particle concentration is a result of a balance between turbulent suspension and gravitational settling. Thus in the absence of particle inertia, Eq. 9 accurately predicts concentrations over a range of settling velocities in regions of the flow where turbulence and gravity are indeed the dominant transport mechanisms.

3 Results and Discussion

3.1 Interpretation

The numerical methodology outlined in the previous sections represents an idealized approach towards understanding the role of inertia in the flux-profile relationship of suspended particles. As such, we include here a brief discussion of both the applicability of the following results, as well as an explanation for how they should be interpreted.

Firstly, the lower boundary conditions utilized for both the Eulerian and Lagrangian simulations are not intended to physically represent the process of particle emission from the surface. Since aeolian saltation at the sand/snow surface, droplet formation at the air-sea interface, lifting at the subaqueous sediment layer, for example, have widely varying physical explanations, the focus here is instead on the vertical transport of particles *once they have been suspended*. In the present work, molecular diffusion, as represented by Brownian motion for the Lagrangian particles and by a constant molecular diffusivity for the Eulerian concentration field, is used as a means for achieving this suspension, in the sense that it is responsible for carrying particles from the specified concentration at the surface to a level where turbulence dominates transport (this occurs at a level of $z/H \approx 0.1$ in the DNS presented here). This allows for a direct comparison between the Eulerian and Lagrangian methods, and allows us to focus instead on the turbulent transport in regions above this layer. The means by which the particles have arrived this this height is immaterial for our purposes.

Secondly, the DNS framework is meant to represent only the lowest few metres of the ASL where inertia is present (the "inertial resistance layer"—see Fig. 3). Thus the parameter H in
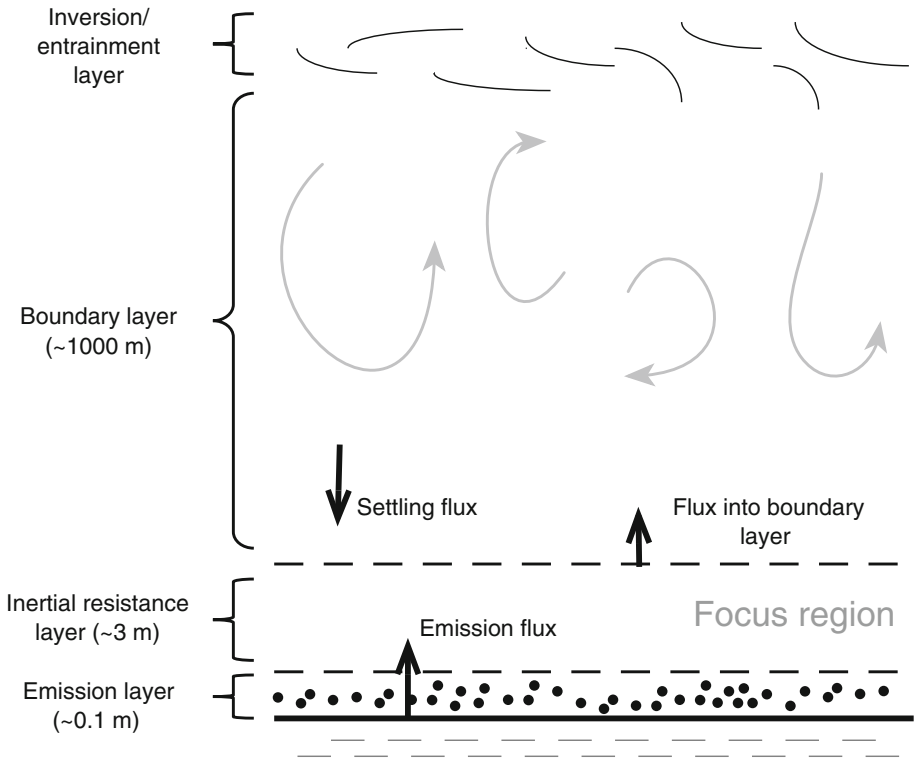
Fig. 3 Schematic detailing the structure of the PBL and the focus of the present DNS study. In the region above the emission layer and below the full boundary layer, local Stokes numbers can be large due to the rapid change in the TKE dissipation rate with height, resulting in inertia-dominated transport of particles in the bottom few metres of the PBL. The emission layer includes the region where processes such as bubble bursting or saltation occur, which are not explicitly represented in this study

the simulations is not the PBL height of $O(1000\,\mathrm{m})$ but rather the top of the inertial resistance layer that has a height of $O(1\,\mathrm{m})$. For a given particle size, the Stokes number computed based on the local Kolmogorov time scale changes very rapidly with height, leaving a region near the surface (but above the emission layer) where inertia effects can be large. The depth of this layer is controlled by both the particle size and the turbulence levels in the PBL. Since $St = \tau_\mathrm{p}/\tau_\mathrm{K}$ depends on both τ_p and the local Kolmogorov time scale, the depth of this layer would scale as d_p^2, since τ_p is proportional to d_p^2, and with $u_*^{3/2}$, since the TKE dissipation rate ϵ is proportional to u_*^3 and τ_K is proportional to $\epsilon^{-1/2}$ (at least in neutral conditions). As demonstrated below in Sect. 3.6, the features observed in the DNS can be felt throughout larger-scale models that cannot resolve these small-scale motions and instead resolve PBL-scale motions.

3.2 Adding Particle Inertia

Our goal is to extend the analysis of Sect. 2.2 to include particles that exhibit appreciable inertia during their turbulent transport. In most studies on this topic (Chamberlain 1967; Kind 1992; Chamecki et al. 2009), particle inertia is neglected and only gravitational settling is

taken into consideration. In other studies (Csanady 1963; Belan et al. 2016; Freire et al. 2016), particle inertia is treated insofar as it is responsible for altering dispersion rates, and compared to the large scales associated with the full PBL the effect of inertia is quite small. Here, our focus is on the lowest layers of the particle-laden boundary layer, where the transport is crucial for linking the small-scale emission processes with the large-scale PBL.

With this in mind, we design a set of numerical experiments whose purpose is to systematically vary the particle inertia while holding the settling tendency the same, in order to determine the effects on the average concentration profiles and flux characteristics. A non-dimensional settling velocity of $w_s/(\kappa u_*) = 0.06$ is held fixed (red lines in Fig. 2), and the flow Reynolds number is likewise fixed at $Re_* = 300$. The particle inertial time scale τ_p is then varied to provide Stokes numbers ranging between $St = 0.05$ and 5. We note that the following analysis only reports results from a single non-dimensional settling velocity, but the same general results are found at other values of $w_s/(\kappa u_*)$. The effect of w_s is to modify the baseline concentration profile, from which inertia modifies as described below. We also note that, while holding w_s constant while varying St is artificial, it allows us to target explicitly the effects of inertia, without confounding them with changes in w_s at the same time. In reality, w_s and St are linked via τ_p, although local values of St can change with height.

For our DNS, we use a flow time scale of $\tau_f = \overline{\tau}_K$ to define St, where $\overline{\tau}_K$ is the vertically-averaged Kolmogorov time scale in the channel. For reference, if one uses the logarithmic scaling of viscous dissipation rate in the ASL, $\epsilon = u_*^3/\kappa z$, then $\overline{\tau}_K$ averaged over the lower 5 m of the surface layer for $u_* = 0.4$ m s^{-1} is roughly 0.015 s. In these conditions the Stokes number range of $St = 0.5$ to 5 corresponds to diameters of $d_p \approx 10\,\mu$m to $d_p \approx 150\,\mu$m when the particle density is of order 1000 kg m^{-3}. Thus spray droplets, dust, or snow particles suspended in air can quite easily behave as inertial particles within $O(1\,\text{m})$ of the surface (i.e., the "inertial resistance layer" found in Fig. 3).

Figure 4a presents the normalized average concentration profiles as a function of z/H over the range of St considered. Despite the settling velocity being identical between these cases, the addition of inertia clearly inhibits the ability of particles to distribute vertically throughout the domain. Over the present range of St, this trend is monotonic, in that higher St leads to lower mean concentrations throughout the entire channel. The exception is the $St = 5$ case, where upwards turbophoretic drift (Reeks 1983; Sardina et al. 2012) actually overcomes gravitational settling, pushing particles towards the top wall and increasing concentrations there (i.e., the finite size of the domain begins to contaminate the solution since vertical velocity fluctuations must approach zero at the top wall).

Figure 4b illustrates that the Prandtl theory describing the vertical profiles of concentration as a balance between turbulent flux and gravitational settling fails significantly as St is increased (thin black lines). At low St, Eq. 9 is still accurate in the upper regions of the domain, but the height range over which agreement is found diminishes. The disagreement propagates from the bottom, since the local Stokes number, as computed by the local value of τ_K, is a monotonically decreasing function with height. Thus the first regions of the flow where the theory begins to fail are those where the local St is locally large enough to cause the particles to cease acting as settling, passive tracers.

By solving Eq. 3 and only considering gravitational advection (i.e., $v_j = u_j - w_s\delta_{j3}$), the turbulent flux $\langle c'w' \rangle$, diffusive flux $-\Gamma_C(\partial \langle C \rangle/\partial z)$, and gravitational flux $-w_s \langle C \rangle$ are computed directly from the Eulerian concentration field. Simultaneously, the same flux quantities can be computed from the Lagrangian particles as well. The gravitational flux is still $-w_s \langle C \rangle$ (using the Lagrangian-based $\langle C \rangle$), and Reynolds averaging of the particle evolution equations shows that the sum of the turbulent and gravitational fluxes is equal to $\langle w_p \rangle \langle C \rangle$,
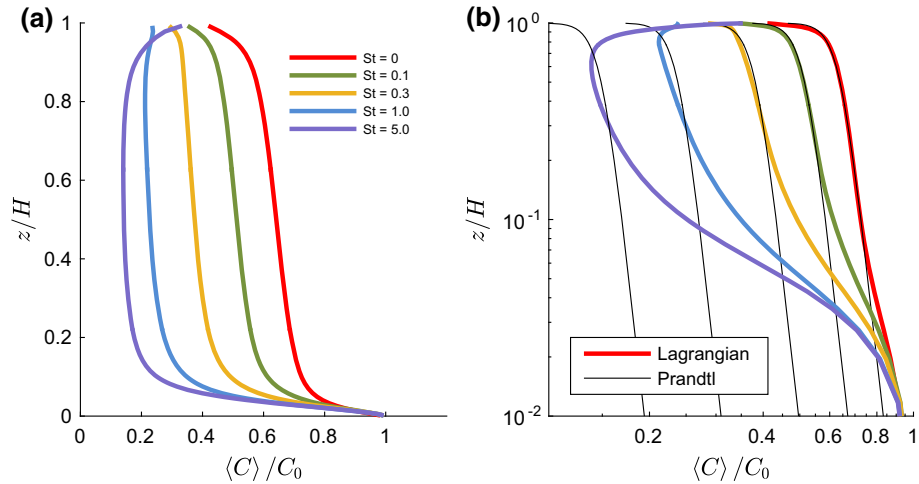
Fig. 4 **a** Average normalized concentration $\langle C \rangle / C_0$ computed from the inertial, Lagrangian simulations as a function of z/H. The settling velocity is held fixed at $w_s/(\kappa u_*) = 0.06$ for all cases, and $Re_* = 300$. **b** The same concentration profiles on logarithmic axes, with Eq. 9 plotted in thin black lines for reference. The addition of inertia dramatically changes the concentration within the domain, and causes the average profile to deviate significantly from the inertialess theory

where $\langle w_p \rangle$ is the average particle vertical velocity. Therefore the turbulent flux (counterpart to $\langle c'w' \rangle$ in the Eulerian frame) is the difference between the gravitational flux and the concentration-weighted average particle velocity. Finally, the total flux is computed from the Lagrangian point of view by keeping track of the net number of particles crossing each horizontal plane in each timestep. From this total, the gravitational and turbulent fluxes can be subtracted to yield the diffusive flux.

First, to demonstrate that the Eulerian versus Lagrangian-based flux calculations are equivalent for systems with no inertia, Fig. 5 shows the Lagrangian-computed profiles in thick red lines and the Eulerian-computed fluxes thin black lines for the inertialess case shown in Fig. 4. It is clear that the flux profiles in this case are nearly identical, and therefore the Lagrangian-based fluxes are accurate representations of vertical particle transport.

Several features are of note in Fig. 5. First, since we average only after the system has reached steady state, the total flux should be zero, which Fig. 5 indeed indicates is the case. Figure 5 shows that in this steady state condition, above $z/H \approx 0.1$ and below $z/H \approx 0.9$, the flux balance, even in the presence of substantial particle inertia, is strictly between gravitational settling and turbulent suspension. As expected, this spatial region corresponds to the region of Fig. 4 where the Prandtl-predicted concentration profile agrees with the simulations in the absence of particle inertia. Near the top and bottom walls, turbulent fluxes are replaced by non-zero diffusive fluxes, thus violating the assumptions behind the Prandtl theory.

Regarding inertial effects, Fig. 5 also illustrates that within the regions unaffected by diffusion, increases in particle inertia suppress turbulent fluxes, which are in turn balanced by lower gravitational settling fluxes. So while the dominant balance remains between turbulence and gravity, their magnitudes have deviated sharply from the non-inertial case. This trend increases with St, and the inertialess Eulerian formulation (thin black lines) is clearly insufficient in predicting the fluxes for inertial particles.
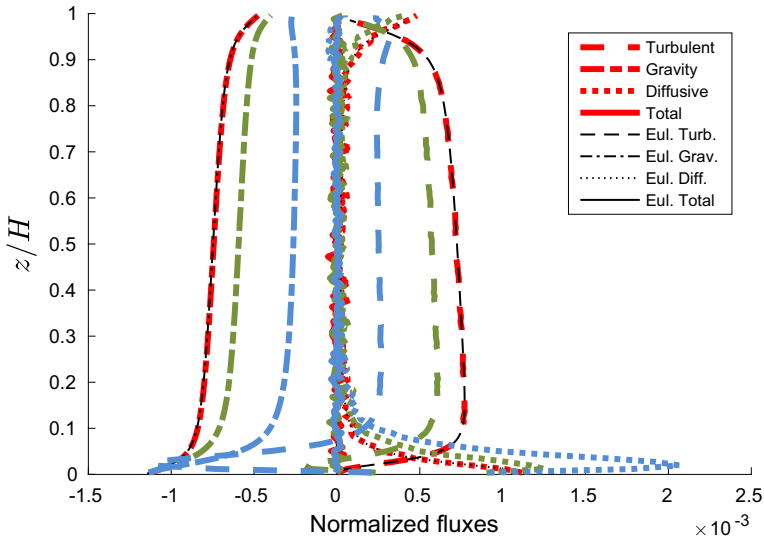
Fig. 5 Vertical profiles of concentration fluxes for a subset of the overall Stokes numbers: $St = 0$ (red), $St = 0.1$ (green), and $St = 1$ (blue). Line types provided in the legend refer to the turbulent flux, the gravitational flux, the diffusive flux, and the total flux. The thick coloured lines refer to fluxes computed from the Lagrangian particle data; thin black lines are fluxes from an Eulerian, inertialess perspective. Fluxes normalized by $C_0 U_0$, where U_0 is the maximum velocity in the channel. The notation "$\times 10^{-3}$" in the bottom right of this and subsequent figures refers to the exponent of the values on the abscissa

3.3 Inertial Correction to the Advection Velocity

In order to capture inertial effects in the Eulerian calculations, we utilize an inertial correction to the advection velocity v_j in Eq. 3 that is based on an asymptotic expansion of Eq. 4 in Stokes number, retaining only the first-order correction (Maxey 1987; Druzhinin 1995). More recent implementations of this correction have acquired the name of the "equilibrium Eulerian" model, whose advantage is that it captures some inertial effects while still allowing the particle advection velocity to be written in terms of local flow velocities and accelerations (Ferry and Balachandar 2001; Balachandar 2009).

Under this approximation, the advection velocity takes the form,

$$v_j = u_j - w_s \delta_{j3} - \tau_p \frac{Du_j}{Dt}, \tag{10}$$

where $\frac{D}{Dt} = \frac{\partial}{\partial t} + u_k \frac{\partial}{\partial x_k}$ is the total fluid acceleration. The meaning of the last term in Eq. 10 is that the fluid velocity seen by the particle at a time τ_p before the present time should be factored into the current particle velocity due to inertia, and would only be expected to be accurate below $St \approx 0.2$ since the correction is only first order (Ferry and Balachandar 2001).

Following the same Reynolds averaging procedure as done for deriving Eq. 7, this correction to the advection velocity leads to two additional terms in the vertical flux balance,

$$\langle c'w' \rangle - \langle C \rangle w_s - \langle C \rangle \tau_p \frac{\partial \langle w'^2 \rangle}{\partial z} - \tau_p \left\langle c' \frac{Dw'}{Dt} \right\rangle = 0. \tag{11}$$
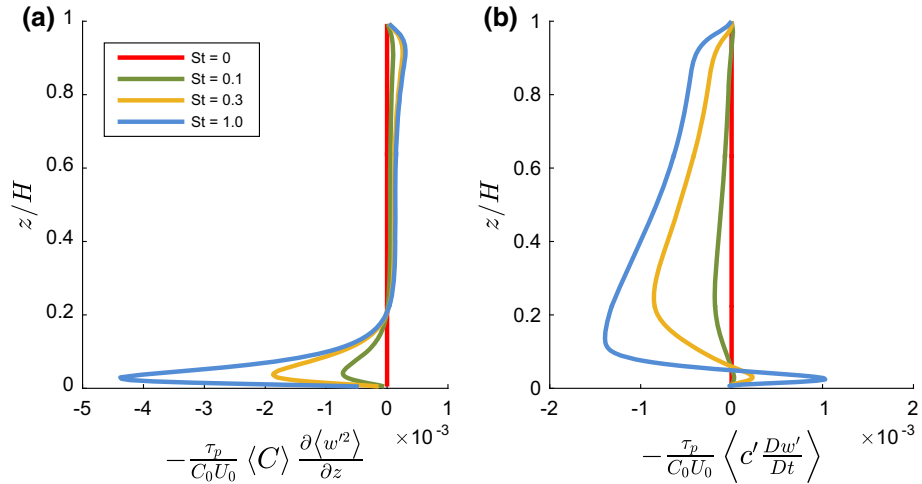
Fig. 6 Additional, inertia-based flux terms in Eq. 11 as a function of height. Different lines refer to different Stokes numbers ranging between 0 and 1 (see legend). **a** turbophoresis term: $-\tau_{\mathrm{p}} \langle C \rangle \frac{\partial \langle w'^2 \rangle}{\partial z}$, **b** correlation between concentration fluctuations and vertical accelerations: $-\tau_{\mathrm{p}} \left\langle c' \frac{Dw'}{Dt} \right\rangle$. Both terms normalized by $C_0 U_0$

The first two terms are the same turbulent and gravitational settling fluxes from Eq. 7; the third term on the left-hand side of Eq. 11 represents turbophoresis, where inertia causes a drift against gradients of TKE (Reeks 1983), and the fourth term on the left-hand side represents correlations between concentration fluctuations and vertical accelerations. It can be easily shown that the sum of these two terms is simply $-\tau_{\mathrm{p}} \left\langle C \frac{Dw'}{Dt} \right\rangle$, i.e., the correlation of the total concentration with vertical acceleration.

With this formulation in mind, we perform a new simulation in which v_j in Eq. 3 is replaced by Eq. 10 in order to compare its predictions with the true behaviour of the inertial Lagrangian particles (here "true" indicates that we expect the theory to match the Lagrangian simulations exactly if the theory were correct). From these calculations, Fig. 6 presents the two extra flux terms in Eq. 11 as a function of height for a range of St, which shows that each of the inertial corrections to the vertical flux are of the same order of magnitude. As expected, the turbophoretic term in Fig. 6a is largest in the regions near the lower wall where the gradients of the turbulent kinetic energy are the highest. These profiles are related to one another, in the sense that the gradient $\frac{\partial \langle w'^2 \rangle}{\partial z}$ is the same in all cases since the underlying turbulence has not changed with particle Stokes number.

In the range where molecular diffusion is unimportant (above $z/H \approx 0.1$), the concentration fluctuation/vertical acceleration correlation term (Fig. 6b) is dominant and negative, suggesting that inertia tends to reduce the vertical flux. This is in agreement with the Lagrangian-based fluxes computed in Fig. 5, and provides an Eulerian interpretation of this suppression of the concentration flux. It is noteworthy that the dominance of this term over the turbophoretic term indicates that inertial corrections to vertical dispersion must include additional effects beyond turbophoretic drift. As the particle Stokes number increases, these flux corrections generally become larger since they are proportional to τ_{p}, although the correlation saturates around $St = 0.5$. We note that the corrections for $St = 5$ are not shown
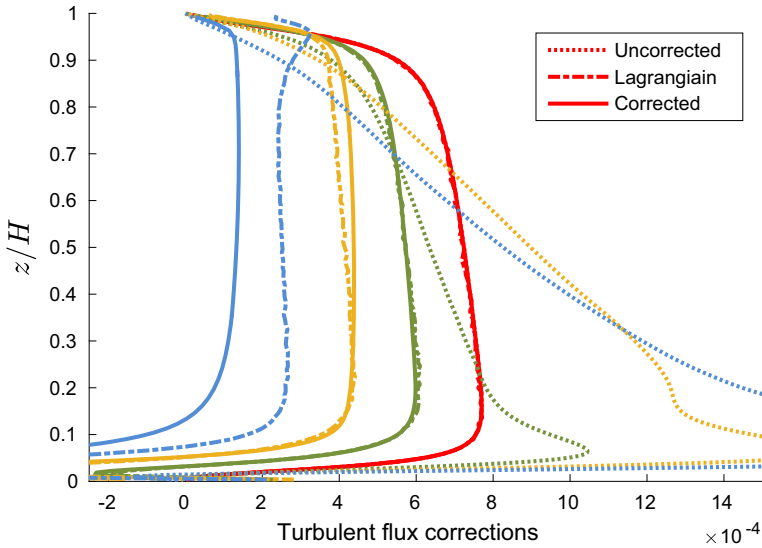
Fig. 7 Turbulent fluxes with inertial correction to Eulerian advection velocity. Uncorrected turbulent flux $\langle c'w' \rangle$ (dashed), Lagrangian turbulent flux (dash-dotted), and the corrected turbulent flux $\langle c'w' \rangle_{corr}$ (solid). Line colours refer to legend in Fig. 6. Axes have been zoomed in to better highlight agreement between the Lagrangian-based fluxes and the corrected Eulerian fluxes

since the inertia-corrected advection velocity causes the numerical simulations to become unstable at such high values of τ_p.

If one interprets the last two terms of Eq. 11 as a correction to the inertialess turbulent flux, then a corrected turbulent flux can be defined,

$$\langle c'w' \rangle_{corr} = \langle c'w' \rangle - \langle C \rangle \, \tau_p \frac{\partial \langle w'^2 \rangle}{\partial z} - \tau_p \left\langle c' \frac{Dw'}{Dt} \right\rangle, \tag{12}$$

which should approach the Lagrangian-computed turbulent flux for the inertial particles presented in Fig. 5. Figure 7 shows that this is indeed the case, however beginning at $St \approx 0.3$ the linear correction begins to break down. In this figure, the turbulent flux $\langle c'w' \rangle$ ("uncorrected" in Fig. 7) far overpredicts the vertical turbulent flux over much of the domain when v_j is modified to include the inertia. When adding the additional flux terms of Eq. 11 to $\langle c'w' \rangle$ ("corrected" in Fig. 7), the vertical turbulent flux nearly exactly matches the true flux predicted from the Lagrangian particles. While the corrected Eulerian flux diverges from the Lagrangian beginning at $St \approx 0.3$, the flux is fairly accurate through $St = 0.5$, suggesting that the key inertial effects on vertical fluxes have been captured by the linear correction to v_j. The resulting predictions of the vertical concentration profiles are likewise accurate up to $St \approx 0.3$, as shown in Fig. 8. The degree of success of inertial correction to v_j is in complete agreement with previous uses of the equlibrium Eulerian model (Ferry and Balachandar 2001).

3.4 Revisiting the Prandtl Theory

The Prandtl solution for concentration (Eq. 9) was derived assuming a balance between turbulent suspension and gravitational settling. Furthermore, it uses a parabolic form of the
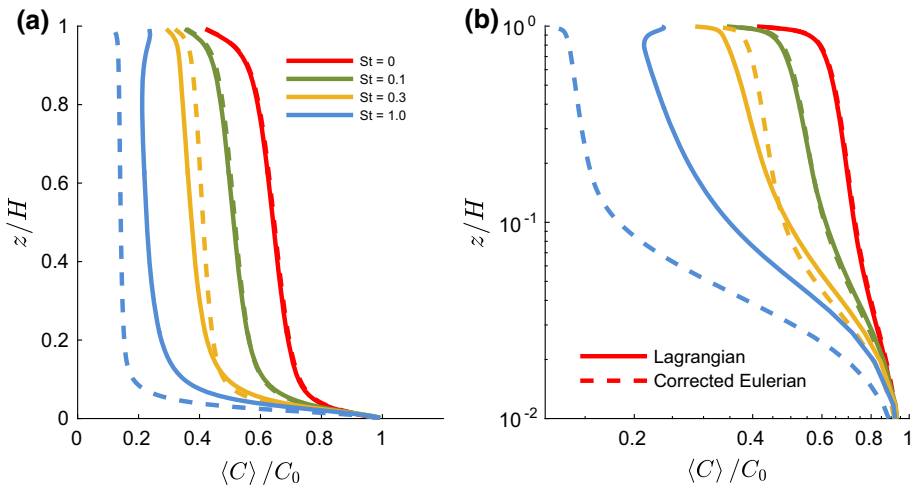
Fig. 8 Concentration profiles as predicted by the Lagrangian particles (solid lines) and the corrected Eulerian field (dashed lines). **a** Linear axes, **b** logarithmic axes

eddy diffusivity, i.e., $K_C = \kappa u_* z \left(1 - z/H\right)$, which is the eddy diffusivity predicted by MO similarity theory in the presence of a linear momentum flux. As a first step, therefore, we compute K_C in the case of inertial particles to see how well a parabolic function compares with the eddy diffusivity implied by the ratio of the turbulent flux to the mean concentration gradient. For the corrected Eulerian flux this follows,

$$K_{C,E} = -\frac{\langle c' w' \rangle_{corr}}{\partial \langle C \rangle / \partial z},\tag{13}$$

while for the Lagrangian-computed turbulent flux K_C is computed as,

$$K_{C,L} = -\frac{\left(\langle w_p \rangle + w_s\right) \langle C \rangle}{\partial \langle C \rangle / \partial z},\tag{14}$$

where the numerator is the turbulent flux measured from the Lagrangian particles, and inherently includes all true inertial effects.

Figure 9 shows both $K_{C,E}$ and $K_{C,L}$, and compares them to the parabolic solution assumed by MO theory. It is clear that the inertialess case ($St = 0$, red lines) follows the parabolic solution fairly closely, which is expected since the Prandtl solution was successful at predicting the mean concentration profiles in Fig. 4. As St increases, however, not only do the computed eddy diffusivities deviate from the parabolic approximation, the Eulerian and Lagrangian predictions deviate from one another. Again, this is expected given the deviation between the corrected Eulerian and Lagrangian profiles shown in Figs. 7 and 8, since the Eulerian correction is only valid at low St. We note that the difference between $K_{C,L}$ and the parabolic solution is not simply a result of the so-called crossing trajectories effect: the correction proposed by Csanady (1963) for the vertical eddy diffusivity results in a vertical dispersion coefficient that is less than 1% different than the parabolic solution.

While the shape of both $K_{C,E}$ and $K_{C,L}$ is close to parabolic at $St = 0.3$ (yellow lines in Fig. 9), the emergence of an inflection point in the concentration profile at $St = 1$ (see Fig. 8) causes $K_{C,L}$ to spike to very large and even negative numbers near $z/H \approx 0.8$. This behaviour indicates that inertial particles violate the basic flux-gradient relationship assumed when
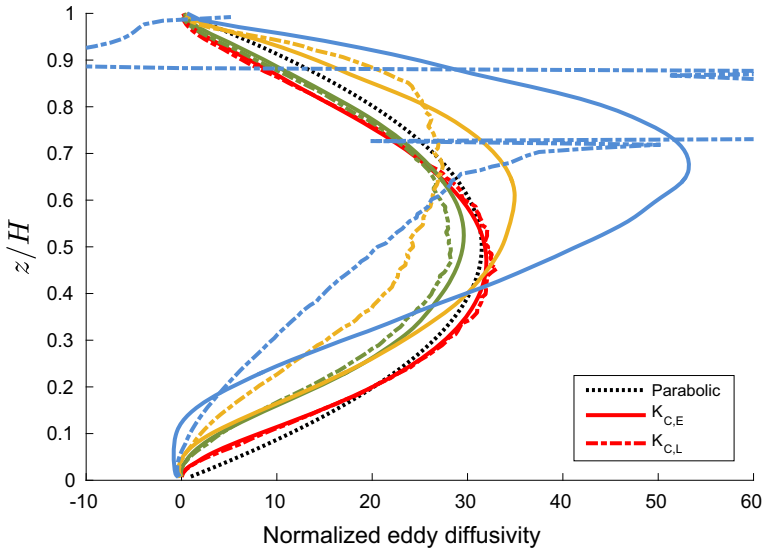
Fig. 9 Eddy diffusivities normalized by the molecular diffusivity Γ_C. Dotted black line represents the parabolic solution $K_C = \kappa u_* z\,(1 - z/H)$. Solid lines represent $K_{C,E}$ and dash-dotted lines represent $K_{C,L}$. Both profiles have been smoothed with an averaging filter. Colours follow the legend of Fig. 8

defining an eddy diffusivity K_C, although the inertial correction to the Eulerian advection velocity compensates for this up to $St \approx 0.2$, as noted earlier.

It is instructive therefore to repeat the Prandtl analysis and attempt to predict the concentration profile while incorporating the inertial corrections to the Eulerian concentration field. The goal here is to determine whether or not a parabolic eddy diffusivity can be utilized for the uncorrected turbulent flux $\langle c'w' \rangle$ while capturing the inertial effects separately and explicitly. If this fails (which it indeed does), it would indicate that inertial effects must be accounted for in the eddy diffusivity itself and not as a series of correction terms to the overall flux balance. If Eq. 11 is written as

$$\langle c'w' \rangle - \langle C \rangle\, w_s + \beta(z) = 0, \tag{15}$$

where $\beta(z)$ represents the inertial corrections to the turbulent flux,

$$\beta(z) = -\langle C \rangle\, \tau_p \frac{\partial \langle w'^2 \rangle}{\partial z} - \tau_p \left\langle c' \frac{Dw'}{Dt} \right\rangle, \tag{16}$$

the analogue to Eq. 8 assuming the parabolic form of the eddy diffusivity K_C is

$$\kappa u_* z\,(1 - z/H) \frac{d \langle C \rangle}{dz} + \langle C \rangle\, w_s = \beta(z). \tag{17}$$

The solution to this inhomogeneous equation takes the form

$$
\begin{aligned}
\frac{\langle C \rangle\,(z)}{C_r} =& \left(\frac{z}{z_r} \right)^{-w_s/\kappa u_*} \left(\frac{z - H}{z_r - H} \right)^{w_s/\kappa u_*} \\
&+ \left(\frac{z}{H - z} \right)^{-w_s/\kappa u_*} \int_{z_r}^{z} \left(\frac{z}{H - z} \right)^{w_s/\kappa u_*} \frac{\beta(z)}{C_r \kappa u_* z\,(1 - z/H)}\, dz,
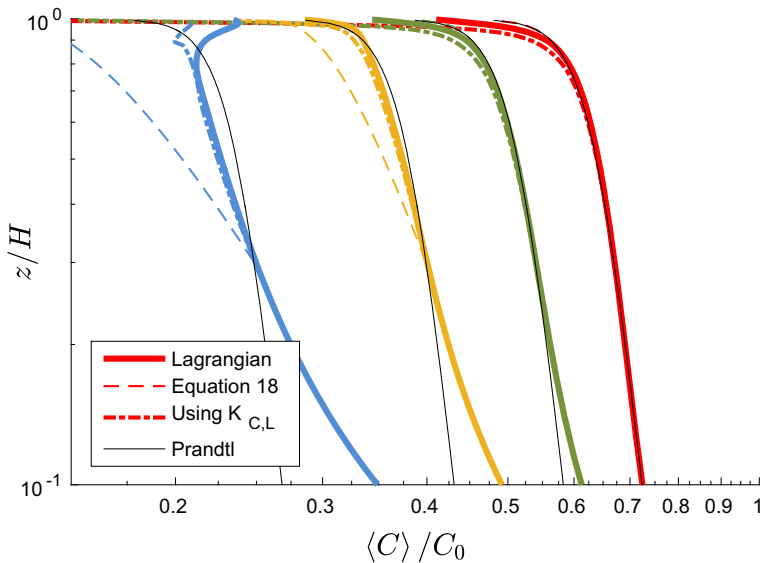\end{aligned} \tag{18}
$$

Fig. 10 Vertical concentration profiles computed from the inertial Lagrangian particles (solid lines) compared to the prediction of Eq. 18 (dashed lines). As before, $z_r = 0.3H$ and C_r is the concentration at this height, so the solution to Eq. 18 only exists above $z/H = 0.3$. Dash-dotted lines are the numerical solutions to Eq. 19, which uses the Lagrangian-based $K_{C,L}$, illustrating that the parabolic K_C becomes insufficient at high St. Colours refer to the legend in Fig. 8

which contains the original Prandtl solution of Eq. 9 as the first term, followed by a correction which involves an integral of the inertial correction term $\beta(z)$. Since we do not have a closure for this term, we must integrate this term numerically, and its solution is presented in Fig. 10. Note that since $\langle C \rangle$ appears in the definition of $\beta(z)$, the numerical solution must be iterative; since the term containing $\langle C \rangle$ is small above $z_r = 0.3$ (Fig. 6a), however, the solution converges very rapidly.

Figure 10 shows that the correction indicated by Eq. 18 does not adequately modify the original Prandtl solution to account for inertia. This is of course true at the highest values of St (since again the inertial correction only is valid at low St), but even at $St = 0.3$ the additional term in Eq. 18 overcorrects the Prandtl solution substantially.

The reason behind this discrepancy is that the similarity-based, parabolic form of the eddy diffusivity K_C is no longer valid as St increases. If Eq. 8 is written using the Lagrangian-based $K_{C,L}$ as

$$- K_{C,L} \frac{d \langle C \rangle}{dz} - \langle C \rangle w_s = 0, \tag{19}$$

then the solution for $\langle C \rangle$ can be computed numerically using the $K_{C,L}$ profiles presented in Fig. 9 (i.e., the dash-dotted lines). Note that Eq. 19 does not contain the inertial correction term $\beta(z)$ since the Lagrangian-based $K_{C,L}$ inherently includes all inertial effects. Figure 10 shows that when solving Eq. 19, the predicted concentration profile very closely matches the Lagrangian-based concentration profiles, except for regions near the inflection points in $\langle C \rangle$ where $K_{C,L}$ is ill-defined. Thus, the effects of particle inertia on vertical dispersion must not be limited to corrections to the turbulent flux (e.g., using the equilibrium Eulerian model to correct the particle advection
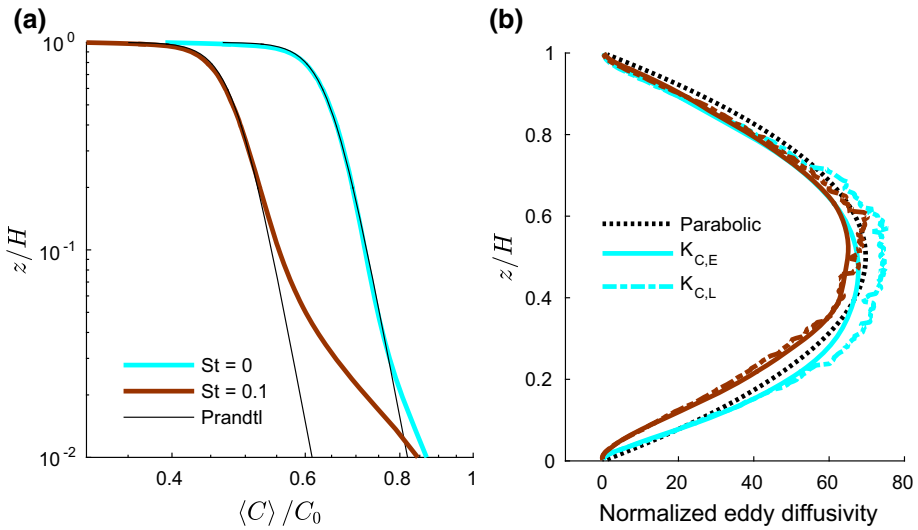
Fig. 11 **a** Concentration profiles and **b** eddy diffusivity profiles for $Re_\tau = 700$ cases for $St = 0$ (cyan) and $St = 0.1$ (dark red) particles. The trends are nearly identical to those presented in Figs. 4b and 9, respectively, illustrating the robustness of the present conclusions with increasing Re

velocity), but must also consider the fact that the eddy diffusivity, and therefore the relationship between the flux and the mean concentration gradient, is modified by inertia as well.

3.5 Reynolds Number

Before demonstrating the effect of the inertial resistance layer in larger-scale models, we provide a comment upon the usage of direct numerical simulation, and thus the limitation in Reynolds number, in the current work. As the Reynolds number of this type of simulation increases towards the types of atmospheric flows we aim to investigate, the primary effect is to reduce the region over which molecular momentum and scalar diffusion dominate; indeed it is only outside of this region that the present work has focused. To this end, two additional simulations were made at a Reynolds number of $Re_* = 700$ in order to demonstrate that our primary conclusions remain intact. Figure 11 shows the counterparts to Figs. 4b and 9 for an inertialess and a $St = 0.1$ particle at the same dimensionless settling velocity. Figure 11a shows that again, the inclusion of particle inertia causes a reduction in the concentration profile, and that the deviation from the Prandtl solution propagates from the lower wall upwards, beginning in regions with high local St. The only difference with the increased Reynolds number is that the range of agreement of the $St = 0$ case with the Prandtl solution extends further towards the lower surface, to $z/H \approx 0.02$ as opposed to $z/H \approx 0.08$ as before. The same is true in Fig. 11b: the presence of inertia begins to alter the eddy diffusivity profile in a similar way to that of the lower Re cases, only in this case the magnitude of K_C is larger (as expected). Thus we argue that the methodology of using DNS as a tool for studying inertial particle fluxes in the lowest regions of the ASL is justified in that the effects of Reynolds number do not appreciably alter our basic findings.
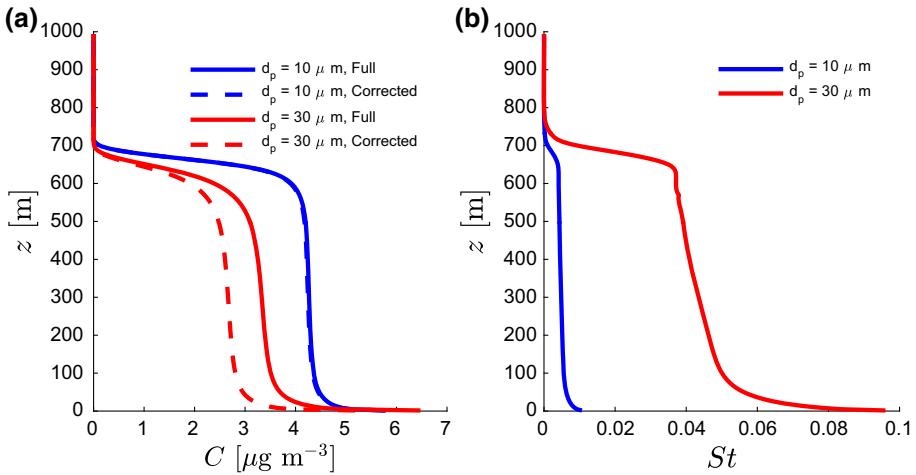
Fig. 12 **a** Concentration profiles of $d_p = 10\,\mu m$ (blue) and $d_p = 30\,\mu m$ (red) particles for the unstable convective PBL of Freire et al. (2016). Solid curves represent full surface fluxes of $0.2\,\mu g\,m^{-2}\,s^{-1}$ and dashed lines represent surface fluxes corrected for inertial transport between the first grid point and the emission layer. **b** Stokes numbers of $d_p = 10\,\mu m$ and $d_p = 30\,\mu m$ particles, as computed by the subgrid dissipation of the LES scheme. From the perspective of LES, these particles are nearly inertialess, but can have significant inertial effects near the surface

3.6 Consequence of the Inertial Resistance Layer

We argue above that within the first few metres above the emission layer, particles often experience inertial effects as they are carried upwards by turbulent motions. In our DNS this is manifested as a reduction of the concentration profile at steady state, but can also be described as a reduction in the vertical turbulent flux above a particle source, similar to classic descriptions of the deposition velocity and transfer resistance via molecular diffusion or vegetation canopies (Slinn and Slinn 1980). This reduction in turbulent flux near the surface occurs even before a steady state has been achieved (i.e., not only in net-zero-flux conditions), and in practice, this effectively reduces the emission flux into the PBL as compared to the true source flux. In the present study we use DNS to resolve these near-wall motions to study their effect, but in practice these motions cannot be resolved and thus their effect must be parametrized.

To demonstrate this process, we perform a representative LES using the unstable convective PBL studied in Freire et al. (2016). For an initial PBL height of $z_i = 570\,m$, a surface heat flux of $0.24\,K\,m\,s^{-1}$, and a geostrophic wind speed of $U_g = 10\,m\,s^{-1}$, Eulerian concentration fields of $d_p = 10\,\mu m$ and $d_p = 30\,\mu m$ particles are solved, only taking into account gravitational settling and not explicitly accounting for inertia. Note that this is not intended to mimic the DNS except on a larger domain—the LES is not steady state (i.e., there is net erosion) and the PBL is under convective conditions. Instead, we intend to show the effects found from our DNS on more typical conditions in the atmosphere, now taking into consideration the inertial behaviour that would not be resolved in LES.

In Fig. 12a, the solid curves represent the concentration profiles averaged between hours 3 and 4 for the same surface emission flux of $0.2\,\mu g\,m^{-2}\,s^{-1}$. As expected, the heavier particles have lower concentrations throughout the PBL. To account for inertial effects at and beneath the first LES grid point, we estimate a surface Stokes number based on LES dissipation at the

first grid point, and use Fig. 7 to provide a corresponding reduction in the surface flux due to the inertial resistance layer. For the case of $d_p = 10\,\mu m$ particles, the local Stokes number at the bottom grid point is $St \approx 0.01$ and the corrected flux is estimated to be 99% of the original surface flux; the dashed blue line in Fig. 12a reflects this small difference. For the case of $d_p = 30\,\mu m$ (dashed red line), however, the surface Stokes number is $St \approx 0.1$ and the reduction in surface flux is roughly 22%. Figure 12a highlights the fact that, as a result of this near-surface reduction of turbulent flux, mean concentrations throughout the entire PBL are influenced by inertia near the surface. Furthermore, Fig. 12b shows that, while inertial effects can lead to substantial changes in the predicted large-scale concentrations, particles in these regions do indeed appear nearly inertialess at these scales, as computed by their local Stokes number. Only near the surface do particles begin to experience inertial effects, even possibly throughout the surface layer (see for example Nemes et al. 2017). We again emphasize that our region of interest, as simulated by DNS, is within several metres of the surface (Fig. 3). By definition, LES in general cannot resolve the observed inertial behaviour of the particles because it is a processes that occurs at the smallest scales of the turbulent flow.

4 Conclusions

In our study we seek to better understand the influence of particle inertia on vertical concentration profiles, and in particular the limitations of traditional relationships that are appropriate in low- or zero-inertia conditions (e.g., Prandtl 1952). We utilize direct numerical simulations and Lagrangian point particles in turbulent open-channel flow to explore the ability of inertial corrections to the Eulerian transport equation [i.e., the equilibrium Eulerian model (Ferry and Balachandar 2001)] to capture changes in the turbulent fluxes and concentration profiles. This numerical set-up is meant to provide insight into the lowest $O(1\,m)$ portion of the ASL, where water droplets or sand/dust grains will experience inertial influences on their trajectories between the time they are emitted and the subsequent transport throughout the whole PBL.

We find that while the primary balance governing the concentration of suspended particles remains between turbulent flux and gravitational settling, both fluxes are reduced in magnitude and cause a reduction of particle concentration at a specific height. This reduction in concentration increases with particle Stokes number, and reflects an inability of the particle to be instantaneously transported with the local fluid motion. Up to a Stokes number of approximately $St \approx 0.3$, the equilibrium Eulerian framework provides a viable means for correcting the turbulent flux, and thus can reproduce inertial particle profiles accurately. Above this threshold, however, this first-order correction fails to reproduce behaviour seen by the Lagrangian particles. In all cases, as the Stokes number is increased, the turbulent flux becomes less well represented by a similarity-based eddy diffusivity, and any attempt at parametrizing the vertical turbulent flux must begin with a more accurate description of the effective, inertia-influenced eddy diffusivity.

The result is that numerical weather prediction or large-eddy simulation models, which attempt to predict the transport of spray, dust, snow, etc., may overestimate airborne concentrations if an inertialess, similarity-based theory is used to link traditional emission schemes (e.g., saltation models, sea-spray generation functions) to the flux at the first grid point above the lower surface. Likewise in practice, surface emission parametrizations may underestimate true emission if airborne concentration observations are used to infer surface fluxes. Since

particles must traverse the first several metres of the surface layer before arriving at elevations corresponding to the first grid point in numerical models, they have necessarily experienced some inertial transport along the way. The present results suggest that this inertial behaviour may result in a decrease in vertical fluxes compared to traditional predictions, and that this result could yield errors at least as large as other typical uncertainties in the system.

References

Aliseda A, Cartellier A, Hainaux F, Lasheras JC (2002) Effect of preferential concentration on the settling velocity of heavy particles in homogeneous isotropic turbulence. J Fluid Mech 468:77–105. https://doi.org/10.1017/S0022112002001593

Anderson RS, Haff PK (1988) Simulation of eolian saltation. Science 241:820–823. https://doi.org/10.1126/science.241.4867.820

Baas ACW (2008) Challenges in aeolian geomorphology: investigating aeolian streamers. Geomorphology 93:3–16. https://doi.org/10.1016/j.geomorph.2006.12.015

Balachandar S (2009) A scaling analysis for pointparticle approaches to turbulent multiphase flows. Int J Multiph Flow 35(9):801–810. https://doi.org/10.1016/j.ijmultiphaseflow.2009.02.013

Balachandar S, Eaton JK (2010) Turbulent dispersed multiphase flow. Annu Rev Fluid Mech 42:111–133. https://doi.org/10.1146/annurev.fluid.010908.165243

Belan S, Lebedev V, Falkovich G (2016) Particle dispersion in the neutral atmospheric surface layer. Boundary-Layer Meteorol 159:23–40. https://doi.org/10.1007/s10546-015-0108-7

Chamberlain AC (1967) Transport of Lycopodium spores and other small particles to rough surfaces. Proc R Soc 296(444):45–70. https://doi.org/10.1098/rspa.1974.0120

Chamecki M, Meneveau C (2011) Particle boundary layer above and downstream of an area source: scaling, simulations, and pollen transport. J Fluid Mech 683:1–26. https://doi.org/10.1017/jfm.2011.243

Chamecki M, Meneveau C, Parlange MB (2009) Large eddy simulation of pollen transport in the atmospheric boundary layer. J Aerosol Sci 40:241–255. https://doi.org/10.1016/j.jaerosci.2008.11.004

Csanady GT (1963) Turbulent diffusion of heavy particles in the atmosphere. J Atmos Sci 20:201–208. https://doi.org/10.1175/1520-0469(1963)020<0201:TDOHPI>2.0.CO;2

Druzhinin OA (1995) On the two-way interaction in two-dimensional particle-laden flows: the accumulation of particles and flow modification. J Fluid Mech 297:49–76. https://doi.org/10.1017/S0022112095003004

Fairall CW, Larsen SE (1984) Dry deposition, surface production and dyamics of aerosols in the marine boundary layer. Atmos Environ 18(1):69–77

Ferry J, Balachandar S (2001) A fast Eulerian method for disperse two-phase flow. Int J Multiph Flow 27:1199–1226. https://doi.org/10.1016/S0301-9322(00)00069-0

Fischer HB (1973) Longitudinal dispersion and turbulent mixing in open-channel flow. Annu Rev Fluid Mech 5:59–78. https://doi.org/10.1146/annurev.fl.05.010173.000423

Freire LS, Chamecki M, Gillies JA (2016) Flux-profile relationship for dust concentration in the stratified atmospheric surface layer. Boundary-Layer Meteorol 160:249–267. https://doi.org/10.1007/s10546-016-0140-2

Groot Zwaaftink CD, Diebold M, Horender S, Overney J, Lieberherr G, Parlange MB, Lehning M (2014) Modelling small-scale drifting snow with a Lagrangian stochastic model based on large-eddy simulations. Boundary-Layer Meteorol 153:117–139. https://doi.org/10.1007/s10546-014-9934-2

Helgans B, Richter DH (2016) Turbulent latent and sensible heat flux in the presence of evaporative droplets. Int J Multiph Flow 78:1–11. https://doi.org/10.1016/j.ijmultiphaseflow.2015.09.010

Hoppel WA, Frick GM, Fitzgerald JW (2002) Surface source function for sea-salt aerosol and aerosol dry deposition to the ocean surface. J Geophys Res 107(D19):1–17. https://doi.org/10.1029/2001JD002014

Kind RJ (1992) One-dimensional aeolian suspension above beds of loose particles—a new concentration-profile equation. Atmos Environ 26(5):927–931. https://doi.org/10.1016/0960-1686(92)90250-O

Kleefeld C, O'Dowd CD, O'Reilly S, Jennings SG, Aalto P, Becker E, Kunz G, de Leeuw G (2002) Relative contribution of submicron and supermicron particles to aerosol light scattering in the marine boundary layer. J Geophys Res 107(D19):8103. https://doi.org/10.1029/2000JD000262

Knippertz P, Todd MC (2012) Mineral dust aerosols over the Sahara: meteorological controls on emission and transport and implications for modeling. Rev Geophys 50:RG1007. https://doi.org/10.1029/2011RG000362

Kok JF (2011) A scaling theory for the size distribution of emitted dust aerosols suggests climate models underestimate the size of the global dust cycle. Proc Natl Acad Sci 108(3):1016–1021. https://doi.org/10.1073/pnas.1014798108

Lewis ER, Schwartz SE (2004) Sea salt aerosol production: mechanisms, methods, measurements, and models–a critical review. American Geophysical Union, Washington

Maxey MR (1987) The gravitational settling of aerosol particles in homogeneous turbulence and random flow fields. J Fluid Mech 174:441–465. https://doi.org/10.1017/S0022112087000193

Monin AS, Yaglom AM (1971) Statistical fluid mechanics, vol 1. Dover Publications Inc., Cambridge

Nemes A, Dasari T, Hong J, Guala M, Coletti F (2017) Snowflakes in the atmospheric surface layer: observation of particleturbulence dynamics. J Fluid Mech 814:592–613. https://doi.org/10.1017/jfm.2017.13

O'Dowd CD, de Leeuw G (2007) Marine aerosol production: a review of the current knowledge. Philos Trans R Soc 365:1753–1774. https://doi.org/10.1098/rsta.2007.2043

Pan Y, Chamecki M, Isard SA (2013) Dispersion of heavy particles emitted from area sources in the unstable atmospheric boundary layer. Boundary-Layer Meteorol 146(2):235–256. https://doi.org/10.1007/s10546-012-9753-2

Peters K, Eiden R (1992) Modelling the dry deposition velocity of aerosol particles to a spruce forest. Atmos Environ 26(14):2555–2564. https://doi.org/10.1016/0960-1686(92)90108-W

Pomeroy JW, Male DH (1992) Steady state suspension of snow. J Hydrol 136:275–301. https://doi.org/10.1016/0022-1694(92)90015-N

Prandtl L (1952) Essentials of fluid dynamics with applications to hydraulics, aeronautics, meteorology, and other subjects. Hafner Publishing Company, New York

Reeks MW (1983) The transport of discrete particles in inhomogeneous turbulence. J Aerosol Sci 14(6):729–739. https://doi.org/10.1016/0021-8502(83)90055-1

Reid JS, Brooks B, Crahan KK, Hegg DA, Eck TF, O'Neill N, de Leeuw G, Reid EA, Anderson KD (2006) Reconciliation of coarse mode sea-salt aerosol particle size measurements and parameterizations at a subtropical ocean receptor site. J Geophys Res 111(D02):202. https://doi.org/10.1029/2005JD006200

Richter DH, Sullivan PP (2013) Momentum transfer in a turbulent, particle-laden Couette flow. Phys Fluids 25(053):304. https://doi.org/10.1063/1.4804391

Richter DH, Sullivan PP (2014) The sea spray contribution to sensible heat flux. J Atmos Sci 71(2):640–654. https://doi.org/10.1175/JAS-D-13-0204.1

Righetti M, Romano GP (2004) Particle-fluid interactions in a plane near-wall turbulent flow. J Fluid Mech 505:93–121. https://doi.org/10.1017/S0022112004008304

Rosenberg PD, Parker DJ, Ryder CL, Marsham JH, Garcia-Carreras L, Dorsey JR, Brooks IM, Dean AR, Crosier J, McQuaid JB, Washington R (2014) Quantifying particle size and turbulent scale dependence of dust flux in the Sahara using aircraft measurements. J Geophys Res Atmos 119:7577–7598. https://doi.org/10.1002/2013JD021255

Rosenfeld D, Lohmann U, Raga GB, O'Dowd CD, Kulmala M, Fuzzi S, Reissell A, Andreae MO (2008) Flood or drought: how do aerosols affect precipitation? Science 321:1309–1313. https://doi.org/10.1126/science.1160606

Rouse H (1937) Modern conceptions of the mechanics of fluid turbulence. Am Soc Civil Eng Trans 102:463–505

Rouson DWI, Eaton JK (2001) On the preferential concentration of solid particles in turbulent channel flow. J Fluid Mech 428:149–169. https://doi.org/10.1017/S0022112000002627

Sardina G, Schlatter P, Brandt L, Picano F, Casciola CM (2012) Wall accumulation and spatial localization in particle-laden wall flows. J Fluid Mech 699:50–78. https://doi.org/10.1017/jfm.2012.65

Slinn SA, Slinn WGN (1980) Predictions for particle deposition on natural waters. Atmos Environ 14:1013–1016. https://doi.org/10.1016/0004-6981(80)90032-3

Slinn WGN (1982) Predictions for particle deposition to vegetative canopies. Atmos Environ 16(7):1785–1794. https://doi.org/10.1016/0004-6981(82)90271-2

Soldati A, Marchioli C (2009) Physics and modelling of turbulent particle deposition and entrainment: review of a systematic study. Int J of Multiph Flow 35:827–839. https://doi.org/10.1016/j.ijmultiphaseflow.2009.02.016

Spalart PR, Moser RD, Rogers MM (1991) Spectral methods for the Navier–Stokes equations with one infinite and two periodic directions. J Comput Phys 96:297–324. https://doi.org/10.1016/0021-9991(91)90238-G

Toba Y (1965) On the giant sea-salt particles in the atmosphere I. General features of the distribution. Tellus 17(1):131–145. https://doi.org/10.1111/j.2153-3490.1965.tb00202.x

Vreman AW (2015) Turbulence attenuation in particle-laden flow in smooth and rough channels. J Fluid Mech 773:103–136. https://doi.org/10.1017/jfm.2015.208

Wang LP, Maxey MR (1993) Settling velocity and concentration distribution of heavy particles in homogeneous isotropic turbulence. J Fluid Mech 256:27–68. https://doi.org/10.1017/S0022112093002708

Wang LP, Stock DE (1993) Dispersion of heavy particles by turbulent motion. J Atmos Sci 50(13):1897–1913. https://doi.org/10.1175/1520-0469(1993)050<1897:DOHPBT>2.0.CO;2

Zhang L, Gong S, Padro J, Barrie L (2001) A size-segregated particle dry deposition scheme for an atmospheric aerosol module. Atmos Environ 35(3):549–560. https://doi.org/10.1016/S1352-2310(00)00326-5